

# Toroidal L and H equilibria with axisymmetric rotations

K.H. Tsui

Instituto de Física - Universidade Federal Fluminense,  
Campus da Praia Vermelha, Av. General Milton Tavares de Souza s/n,  
Gragoatá, 24.210-346, Niterói, Rio de Janeiro, Brasil.

tsui@if.uff.br

Received \_\_\_\_\_; accepted \_\_\_\_\_

## ABSTRACT

Axisymmetric toroidal equilibria with toroidal and poloidal rotations are solved with a specific set of source functions. The two independent solutions are associated to L and H modes. The L/H transition is regarded as a bifurcation from one equilibrium configuration to another, under strong external heating and pellet injection to shape temperature and density profiles. Because of the steep edge gradient of the H solution, large static radial electric field, zonal flow, and improved confinements, come as consequences, not causes, of the H mode.

*Subject headings:* Toroidal Equilibria

## I. INTRODUCTION

The discovery of the H mode with enhanced confinement in ASDEX [1] had opened a new age of tokamak fusion research. Extensive experimental works were performed to identify the key procedures and signatures that carried the L to the H confinement mode [2,3]. These procedures included pellet injection for density enhancement, neutral beam or radio frequency heating for temperature and electric conductivity profiling, etc [4,5]. The experimental signatures of L/H transition were a drastic reduction of the  $D_\alpha$  hydrogen emission and a sudden decrease of the plasma floating potential. These were accompanied by a good enhancement of plasma density and energy confinements, plus a steepening of the edge plasma profile and a reduction of magnetohydrodynamic (MHD) activities [6,7]. Observationally, the L/H transition was accompanied by an increase in the toroidal and poloidal rotations [3]. Nevertheless, it was not clear that this velocity increase was the cause or was the consequence of the transition.

The L/H transition is believed to be caused by divertor shaping of the edge plasma, under high levels of heating power. Action of the divertor plus the edge gradient pump up the static radial electric field that drives a zonal flow near the edge rational magnetic surface [8,9]. This zonal flow is thought to cause a transport barrier that enhances density and energy confinements. The plasma is thought to self-organize gradually under this scenario to reach the H mode [10]. Here, we take a different approach to view the L/H transition. We consider the toroidal and poloidal rotations on the equilibrium scaling, not transport scaling, as equilibrium parameters. We solve for rotational equilibria, under specific source functions, in spherical coordinates by seeking toroidal solutions [11]. There are two independent solutions for rotational equilibrium, and we associate them to the L and H modes. Under this equilibrium configuration approach, the transition is seen

as a bifurcation from one equilibrium to another, under external drivings such as pellet injection for plasma density and strong heating for temperature profiling. Because of the steep edge gradient of the H mode, the large static radial electric field, the zonal flow, and the associated confinements, come as the natural consequences, not causes, of the H mode solution.

## II. ROTATIONAL EQUILIBRIA

To discuss rotational equilibria, we begin with the time-dependent MHD equations

$$\frac{\partial \rho}{\partial t} + \nabla \cdot (\rho \vec{v}) = 0 , \quad (1)$$

$$\rho \left\{ \frac{\partial \vec{v}}{\partial t} + (\vec{v} \cdot \nabla) \vec{v} \right\} = \vec{J} \times \vec{B} - \nabla p , \quad (2)$$

$$\frac{\partial \vec{B}}{\partial t} = -\nabla \times \vec{E} = \nabla \times (\vec{v} \times \vec{B}) , \quad (3)$$

$$\nabla \times \vec{B} = \mu \vec{J} , \quad (4)$$

$$\nabla \cdot \vec{B} = 0 , \quad (5)$$

$$p = \rho v_s^2 . \quad (6)$$

Here,  $\rho$  is the mass density,  $p$  is the plasma pressure,  $\vec{v}$  is the bulk velocity,  $\vec{J}$  is the current density,  $\vec{B}$  is the magnetic field,  $v_s$  is the ion acoustic speed,  $\mu$  is the free space permeability.

With axisymmetry, the magnetic field and the current density can be represented by two scalar functions in standard spherical coordinates

$$\vec{B} = A_0 (\nabla P \times \nabla \phi + Q \nabla \phi) = \frac{A_0}{r \sin \theta} \left\{ +\frac{1}{r} \frac{\partial P}{\partial \theta}, -\frac{\partial P}{\partial r}, +Q \right\} , \quad (7)$$

$$\mu \vec{J} = \frac{A_0}{r \sin \theta} \left\{ +\frac{1}{r} \frac{\partial Q}{\partial \theta}, -\frac{\partial Q}{\partial r}, -\frac{\partial^2 P}{\partial r^2} - \frac{1}{r^2} \sin \theta \frac{\partial}{\partial \theta} \left( \frac{1}{\sin \theta} \frac{\partial P}{\partial \theta} \right) \right\} . \quad (8)$$

Here,  $A_0$  carries the physical dimension of poloidal magnetic flux such that  $P$  is a dimensionless function. Also, we can write the axisymmetric poloidal and toroidal rotations as

$$\vec{v} = A'_0 (\nabla P' \times \nabla \phi + Q' \nabla \phi) . \quad (9)$$

Likewise,  $A'_0$  carries the physical dimension of poloidal velocity flux such that  $P'$  is a dimensionless function. With axisymmetry and incompressible fluid condition,  $\nabla \cdot \vec{v} = 0$ , steady state in Eq. 1 requires

$$\begin{aligned} \nabla \rho \cdot \vec{v} &= A'_0 \nabla \rho \cdot (\nabla P' \times \nabla \phi) = A'_0 (\nabla \rho \times \nabla P') \cdot \nabla \phi = 0 \ , \\ \rho &= \rho_0 \rho(P') \ , \end{aligned} \quad (10)$$

which requires the poloidal velocity and the mass density have the same level contours. Here,  $\rho_0$  carries the dimension and amplitude of mass density, and  $\rho(P')$  is a dimensionless function. As for Eq. 3, by Eq. 7 and Eq. 9, we note that  $\vec{v} \times \vec{B}$  would be null and steady state in Eq. 3 would be warranted with

$$P' = \alpha P \ , \quad (11a)$$

$$Q' = \alpha Q \ . \quad (11b)$$

As a result, the velocity field and the magnetic field are parallel, generating an emf-free velocity field

$$\vec{v} = \alpha \frac{A'_0}{A_0} \vec{B} = g \vec{B} \ . \quad (12)$$

With Eq. 4 and Eq. 6, toroidal plasma equilibria of Eq. 2 with full axisymmetric rotations are described by

$$(1 - \mu\rho_0g^2\rho(P))(\nabla \times \vec{B}) \times \vec{B} - \mu\rho_0v_s^2\nabla\rho(P) = \frac{1}{2}\mu\rho_0g^2\rho(P)\nabla B^2 = 0 . \quad (13)$$

We consider the rotational scalar pressure be much smaller than the plasma pressure, thereby giving the second equality in the above equation.

### III. ROTATIONAL GRAD-SHAFRANOV EQUATION

We seek to solve Eq. 13 for toroidal solutions. This equation renders three components. By axisymmetry, the  $\phi$  component contains only the magnetic force, and it is

$$\frac{\partial P}{\partial r} \frac{\partial Q}{\partial \theta} - \frac{\partial P}{\partial \theta} \frac{\partial Q}{\partial r} = 0 , \quad (14a)$$

$$Q(r, \theta) = Q(P(r, \theta)) . \quad (14b)$$

As for the  $\theta$  component, it reads

$$A_0^2 \left\{ \frac{\partial^2 P}{\partial r^2} + \frac{1}{r^2} \sin \theta \frac{\partial}{\partial \theta} \left( \frac{1}{\sin \theta} \frac{\partial P}{\partial \theta} \right) + \frac{1}{2} \frac{\partial Q^2}{\partial P} \right\} = + \left( \frac{v_s}{g} \right)^2 r^2 \sin^2 \theta \frac{\partial}{\partial P} \ln(1 - \mu \rho_0 g^2 \rho(P)) . \quad (15)$$

This equation is the rotational counterpart of the Grad-Shafranov equation of axisymmetric toroidal plasma equilibrium, represented in spherical coordinate system. The three terms on the left side represent the nonlinear force-free field with  $\mu \vec{J} = K(P) \vec{B}$ , where  $K(P) = \partial Q / \partial P$  is a scalar function. This can be verified from Eq. 7 and Eq. 8 when we impose  $\mu \vec{J} = K(P) \vec{B}$ . In particular, we would have the linear force-free field should we take  $Q^2(P) = (aP)^2$  with constant  $K(P) = a$ . The term on the right side is the plasma pressure balance. The magnetic function  $Q^2(P)$  and the mass density  $\rho(P)$  are source functions that need to be specified. This second order partial differential equation has two independent solutions. Finally, the  $r$  component of Eq. 13 reads

$$\begin{aligned} (1 - \mu \rho_0 g^2 \rho(P)) \frac{\partial P}{\partial r} A_0^2 \left\{ \frac{\partial^2 P}{\partial r^2} + \frac{1}{r^2} \sin \theta \frac{\partial}{\partial \theta} \left( \frac{1}{\sin \theta} \frac{\partial P}{\partial \theta} \right) + \frac{1}{2} \frac{\partial Q^2}{\partial P} \right\} \\ = + \left( \frac{v_s}{g} \right)^2 r^2 \sin^2 \theta \frac{\partial}{\partial r} (1 - \mu \rho_0 g^2 \rho(P)) . \end{aligned} \quad (16)$$



Comparing Eq. 16 to Eq. 15, we note that these two equations are identical. The  $r$  component is simply the self-consistent condition of the  $\theta$  component.

To solve Eq. 15 analytically, we take the source functions as

$$Q^2(P) = a^2 P^2 + Q_0^2 , \quad (17a)$$

$$\ln(1 - \mu\rho_0 g^2 \rho(P)) = -P^q , \quad (17b)$$

$$\mu\rho_0 g^2 \rho(P) = 1 - e^{-P^q} .$$

Writing  $P(r, \theta) = R(r)\Theta(\theta)$ , the rotational Grad-Shafranov equation reads

$$\begin{aligned} & r^2 \frac{1}{R} \frac{\partial^2 R}{\partial r^2} + (ar)^2 + \frac{1}{\Theta} \sin \theta \frac{\partial}{\partial \theta} \left( \frac{1}{\sin \theta} \frac{\partial \Theta}{\partial \theta} \right) \\ &= -\frac{v_s^2}{A_0^2 g^2} q (R\Theta)^{q-2} r^4 \sin^2 \theta = -\frac{1}{\alpha^2} \frac{v_s^2}{A_0'^2} q (R\Theta)^{q-2} r^4 \sin^2 \theta . \end{aligned} \quad (18)$$

The variables of this equation could be separated by taking  $q = 1$  to give

$$(1 - x^2) \frac{d^2 \Theta(x)}{dx^2} + n(n+1) \Theta(x) = 0 , \quad (19a)$$

$$r^2 \frac{d^2 R}{dr^2} + [(ar)^2 - n(n+1)] R = -\frac{1}{\alpha^2} \frac{v_s^2}{(A_0' a^2)^2} (ar)^4 \frac{(1-x^2)}{\Theta} = -A_1 (ar)^4 \frac{(1-x^2)}{\Theta} , \quad (19b)$$

where we have denoted  $x = \cos \theta$ , and used  $n(n+1)$  as the separation constant. The factor  $v_s^2/(A_0' a^2)^2$  is proportional to  $v_s^2/v_{pol}^2$ , where  $v_{pol}$  is the average poloidal rotational velocity.

The first equation gives

$$\Theta(x) = (1 - x^2) \frac{dP_n(x)}{dx} = (1 - x^2) , \quad (20)$$

where  $P_n(x)$  is the Legendre polynomial. We have taken  $n = 1$  to get the second equality. As for the second equation, the  $\theta$  dependent part on the right side disappears by having  $n = 1$ . The solution is given by  $R(r) = R_0(r) + R_1(r)$ , where  $R_0(r)$  and  $R_1(r)$  are the homogeneous and particular solutions. The homogeneous solution is described by

$$R_0(r) = arj_n(ar) + \lambda_0 ary_n(ar) , \quad (21)$$

where  $j_n(z)$  and  $y_n(z)$  are the oscillating spherical Bessel functions, and  $\lambda_0$  is a constant. Together with  $A_0$  defined in Eq. 7, there are two constants for  $R_0(r)$ . As for the particular solution, we have

$$\begin{aligned} z^2 \frac{d^2 R_1}{dz^2} + [z^2 - n(n+1)]R_1 &= -A_1 z^4 , \\ R_1(r) &= -A_1 (ar)^2 = -A_1 z^2 . \end{aligned} \quad (22)$$

We note that the homogeneous solutions,  $R_0(r)$  and  $\Theta(x)$ , correspond to the linear or nonlinear force-free solutions of the left side of Eq. 15. The plasma pressure term on the right side appears only in the particular solution,  $R_1(r)$ , that keeps the pressure balance. The homogeneous radial solution is an oscillating function in  $z = ar$ , which has successive maxima, and the homogeneous meridian solution has a lobe peaked at  $x = 0$ . The superposition of the particular radial solution only slightly modifies the homogeneous solutions. We could use the region between  $z = 0$  and the first root of  $j_n(z)$ , with  $n = 1$ , to describe low aspect ratio high  $\beta$  toroidal plasma equilibria.

#### IV. MAGNETIC AND CURRENT STRUCTURES

With the spatial structure solved, the magnetic field components are given by

$$B_r = +\frac{1}{r \sin \theta} \frac{1}{r} \frac{\partial P}{\partial \theta} = -\frac{1}{r^2} R(r) \frac{d\Theta(x)}{dx} , \quad (23a)$$

$$B_\theta = -\frac{1}{r \sin \theta} \frac{\partial P}{\partial r} = -\frac{1}{r} \frac{dR(r)}{dr} \frac{1}{(1-x^2)^{1/2}} \Theta(x) , \quad (23b)$$

$$B_\phi = +\frac{1}{r \sin \theta} Q(P) . \quad (23c)$$

The solution  $R(r)$  vanishes at some  $r$  where we have  $B_r(r) = 0$ . The solution  $\Theta(x)$  also vanishes at some  $x$ . Together they describe the magnetic fields. Within this region of  $(r, x)$ , the topological center defined by  $dR(r)/dr = 0$  and  $d\Theta(x)/dx = 0$  has  $B_r = 0$  and  $B_\theta = 0$ . This is the magnetic axis,  $r = r_*$ , where the magnetic field is entirely toroidal. The field lines about this center are given by

$$\frac{B_r}{dr} = \frac{B_\theta}{rd\theta} = \frac{B_\phi}{r \sin \theta d\phi} . \quad (24)$$

By axisymmetry, the third group is decoupled from the first two groups. For the field lines on an  $(r - \theta)$  plane, we consider the first equality between  $B_r$  and  $B_\theta$  which gives

$$P(r, x) = R(r)\Theta(x) = C . \quad (25)$$

The nested poloidal field lines are given by the contours of  $P(r, x)$  on the  $(r - x)$  plane. At the topological center, we have  $\Theta(x)$  maximum and  $R(r)$  maximum, so that  $P(r, x)$  is maximum. Since  $r \sin \theta$  is the distance of a point on the  $(r - x)$  plane to the  $z$  axis, Eq. 23c

states that the line integral of  $B_\phi$  around the circle on the azimuthal plane is measured by  $2\pi Q$ ,

$$2\pi r \sin \theta B_\phi = 2\pi Q = \mu I_z .$$

This line integral about the axis of symmetry is maximum at the topological center. Also, it is evident that  $Q$  is equivalent to the axial current, where the constant part  $Q_0$  amounts to a uniform component. As for  $P$ , we evaluate the poloidal magnetic flux by integrating Eq. 23b on the  $x = 0$  plane over a cross section to give

$$\int_{r_*}^r 2\pi r B_\theta dr = -2\pi(P(z) - P(z_*)) .$$

As for the current density of Eq. 8, making use of the Grad-Shafranov equation of Eq. 15 gives

$$\mu \vec{J} = \frac{A_0}{r \sin \theta} \left\{ +\frac{1}{r} \frac{\partial Q}{\partial \theta}, -\frac{\partial Q}{\partial r}, +\left(a^2 P - \frac{1}{\alpha^2} \left(\frac{v_s}{A_0}\right)^2 r^2 \sin^2 \theta \frac{\partial}{\partial P} \ln(1 - \mu \rho_0 g^2 \rho(P))\right) \right\} . \quad (26)$$

Analogous to the magnetic field lines, the current density field lines are given by

$$\frac{J_r}{dr} = \frac{J_\theta}{r d\theta} = \frac{J_\phi}{r \sin \theta d\phi} . \quad (27)$$

Considering the first equality, the poloidal current density contours are given by

$$Q(r, x) = C . \quad (28)$$

## V. L AND H MODES

We note that there are two independent solutions for  $R_0(r)$  in Eq. 21. The first one is  $zj_1(z)$  which vanishes at  $z = 0$ . With  $z_1$  and  $z_2$  as the first and second zeros, the region bounded by  $0 < z < z_1$  could be used to describe spheromak and high  $\beta$  low aspect ratio tokamak equilibria. The second one is  $zy_1(z)$  which diverges at  $z = 0$ . Since our domain of interest in tokamak plasmas excludes  $z = 0$ , the singularity of  $y_1$  is irrelevant. The region bounded by  $z_1 < z < z_2$  could also be used to describe high  $\beta$  low aspect ratio tokamak equilibria. The functions  $zj_1(z)$  and  $zy_1(z)$  are shown in Fig.1. The poloidal magnetic contours of Eq. 25 for  $zj_1(z)$  in the interval  $0 < z < z_1$  are shown in Fig.2. In particular, this solution could also be applied to spheromaks where  $z = 0$  is accessible to plasma equilibria. Similar contours for  $z_1 < z < z_2$ ,  $z_2 < z < z_3$ , and so on, can be obtained to represent tokamak plasmas of different aspect ratios. The contours for  $zy_1(z)$  in the interval  $z_1 < z < z_2$  are shown in Fig.3. In order to illustrate the essential features, we have neglected the particular solution  $R_1(r)$ , and have taken  $R(r) = R_0(r)$ . The contour levels are taken at 0.95, 0.9, 0.7, 0.5, 0.3, 0.1 of the respective peak value. The external contours indicate high poloidal fields, and internal contours for low poloidal fields. These contours also indicate the poloidal rotations with rotation velocity high on the outside and low on the inside.

Bounded by a smaller interval  $z_1 < z < z_2$ , we note that Fig.3 of  $zy_1(z)$  has a more localized domain and steeper edge profile than the equilibrium in Fig.2, which is described by  $zj_1(z)$  in the larger interval  $0 < z < z_1$ . Including the negative valued particular solution  $R_1(r)$  further steepens the edge gradient. We associate  $zj_1(z)$  and  $zy_1(z)$  to the L and H mode respectively. We also note that the poloidal and toroidal magnetic fields are plotted in normalized radial coordinate  $z = ar$ . In laboratory plasmas, the fields are

measured in terms of radius  $r$ . To connect to our normalized results, we need to determine the normalizing parameter  $a$ . This can be done by considering the magnetic axis  $r_*$  of a laboratory plasma, say in the  $zj_1(z)$  mode bounded by  $0 < z < z_1$ , through  $a_j r_* = z_* = 2.7$ . Defined by the divertor scrape-off, the radial range of laboratory plasma,  $r_a < r < r_b$ , can now be converted to  $0 < z_a < z < z_b < z_1$  with  $z_1 = 4.5$ . In the case of  $zy_1(z)$  mode, we have  $a_y r_* = z_* = 4.5$ , giving  $a_y/a_j = 4.5/2.7$ . The radial range can be converted to  $z_1 < z_a < z < z_b < z_2$  with  $z_1 = 2.8$  and  $z_2 = 6.1$ . Experimentally, this change of the normalizing parameter from  $a_j$  to  $a_y$  could be accomplished by pellet injection and high power external heating.

In the L mode, the  $zj_1(z)$  profile is more diffused between a larger interval of the zeros. The divertor action removes the edge plasma to the  $z_a < z < z_b$  domain, with poloidal rotation velocity contours corresponding to such domain. In the H mode, due to the compactness of the interval between zeros of  $zy_1(z)$  profile, the plasma equilibrium fits within the toroidal machine vessel naturally with much less divertor shaping. The plasma equilibrium occupies probably the entire domain  $z_1 < z < z_2$ , or a large part of it. As a result, poloidal rotation contours of the H mode cover not just the central part but also the high velocity part on the outside. By going from L to H mode, the rotation contours within the plasma cross-section, defined by the divertor action, are enlarged from a partial central profile to an almost complete profile. Observed at a fixed position at the plasma edge, we would have the impression that the rotation velocity has been speeded up.

The corresponding mass density contours of Eq.(17b) for L and H modes are shown in Fig.4 and Fig.5 respectively. The profiles along  $x = 0$  horizontal cut are shown in Fig.6. Although the two modes are presented in one same figure showing approximately the same dimensionless amplitudes, the physical amplitude and dimension is given by  $\rho_0$  defined in Eq. 10. As a result, the mass density of the H mode could be much larger than that of the

L mode. The essence of Fig.6 is to show the relative shape of the mass density profiles for the two modes. We have suggested the identification of L mode to the  $zj_1(z)$  solution in the  $(0, z_1)$  domain, and H mode to the  $zy_1(z)$  solution in the  $(z_1, z_2)$  domain. To map these  $z$  domains to the same  $r$  domain of machine vessel, We have used two different normalizing parameters  $a_j$  and  $a_y$  for the source function  $Q^2(P)$  of Eq. 17a. Since  $a_y = 1.7a_j$ , this would require a substantial increase of toroidal magnetic field according to Eq. 23c. To avoid this substantial toroidal field enhancement, the H mode could be generated by superimposing the  $zy_1(z)$  solution to the  $zj_1(z)$  solution, without displacing significantly the  $z$  domain. As an example, with  $\lambda_0 = 1$ , the profile of  $(zj_1(z) + zy_1(z))$  is shown in Fig.7 indicating  $z_1 = 1.9$  and  $z_2 = 5.3$  with a maximum at  $z_* = 3.6$ .

## VI. DISCUSSIONS AND CONCLUSIONS

Experimentally, due to the divertor action on the edge plasma, there is an electrostatic field normal to the magnetic surfaces. This field is particularly large in the H mode configuration because of the steep edge gradient. Since the poloidal field lines are described by the  $P$  contours, this field can be written as  $\vec{E} = -\nabla\Phi(P)$ , which warrants  $\partial\vec{B}/\partial t = 0$  for equilibrium. Interacting with magnetic islands on a rational surface, this electric field drives zonal flows that establish transport barriers for better plasma density and energy confinements. With the rotational toroidal equilibrium approach, the L/H transition amounts to a bifurcation of the L equilibrium to the H equilibrium, under the actions of external pumping through pellet injection and strong auxiliary heating for density and temperature profile shaping. The normal electric field, zonal flows, and transport barriers, come as consequences, not causes, of the steep edge gradient of the H mode.

We have solved toroidal plasma equilibria with axisymmetric toroidal and poloidal rotations, that are self-similar to the corresponding magnetic fields. The rotational Grad-Shafranov equation in spherical coordinates is solved for toroidal solutions, under the assumption that the scalar rotational pressure is much less than the plasma pressure. With a specific set of source functions, there are two independent homogeneous radial modes given by  $zj_1(z)$  and  $zy_1(z)$ . The  $zj_1(z)$  mode in the region  $0 < z < z_1$  and the  $zy_1(z)$  mode in the region  $z_1 < z < z_2$  could be applied to current large scale tokamaks. The  $zj_1(z)$  mode has a diffuse edge profile over a larger  $z$  domain, and the  $zy_1(z)$  mode has a steep edge profile over a smaller  $z$  domain. We associate them to the L and H modes respectively. The L/H transition amounts to a bifurcation of one equilibrium configuration to another, following a change of the normalizing parameter from  $a_j$  to  $a_y$ . Experimentally, this change of parameter could be achieved by pellet injection and large external heating.



**REFERENCES**

- 1 -F. Wagner et al, Phys. Rev. Lett. **49**, 1408 (1982).
- 2 -F. Wagner et al, Phys. Rev. Lett. **53**, 1453 (1984).
- 3 -K.H. Burrell et al, Phys. Fluids B **2**, 1405 (1990).
- 4 -K.H. Burrell, Phys. Plasmas **4**, 1499 (1997).
- 5 -P. Gohil et al, Plasma Phys. Control. Fusion **45**, 601 (2003).
- 6 -R.J. Taylor et al, Phys. Rev. Lett. **63**, 2365 (1989).
- 7 -H. Xia, M.G. Shats, and H. Punzmann, Phys. Rev. Lett. **97**, 255003 (2006).
- 8 -Z. Lin, T.S. Halm, W.W. Lee, W.M. Tang, and P.H. Diamond, Phys. Rev. Lett. **83**, 3645 (1999).
- 9 -B. Scott, Phys. Lett. A **320**, 53 (2003).
- 10 -P.N. Guzdar, S.M. Mahajan, and Z. Yoshida, Phys. Plasmas **12**, 032502 (2005).
- 11 -K.H. Tsui, Phys. Plasmas **15**, 112506 (2008).

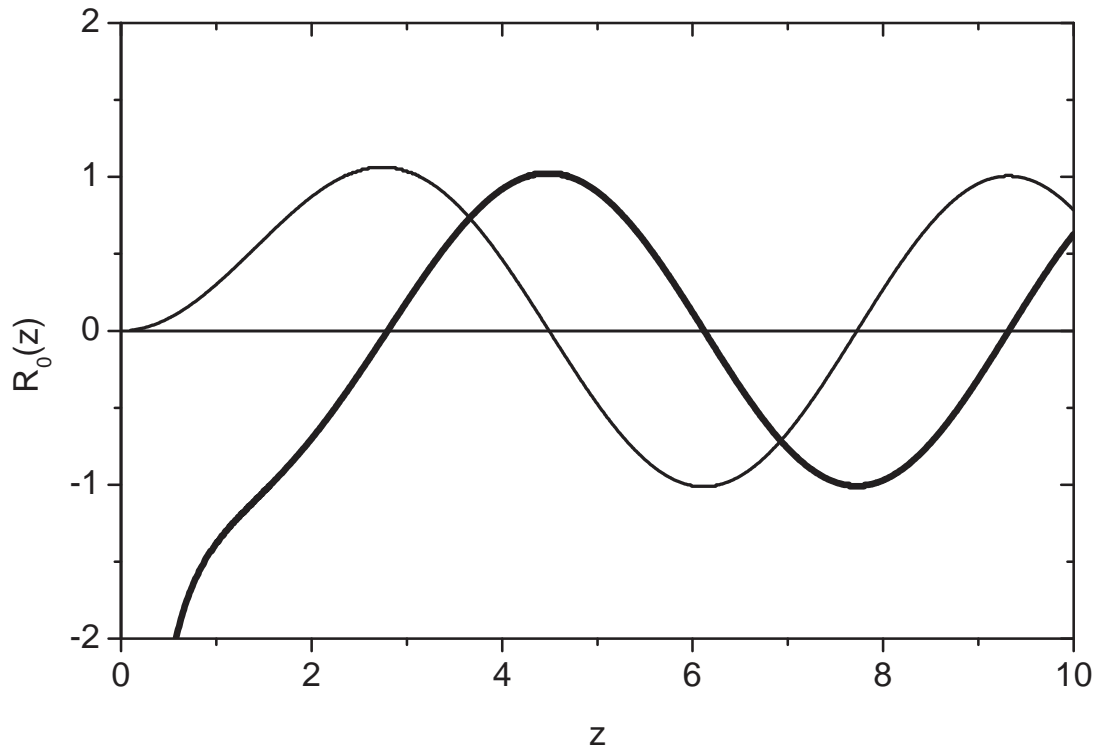


Fig. 1.— The functions  $zj_1(z)$ , in thin line, and  $zy_1(z)$ , in thick line, of the two independent homogeneous  $R_0(z)$  radial solutions are plotted as a function of  $z$ .

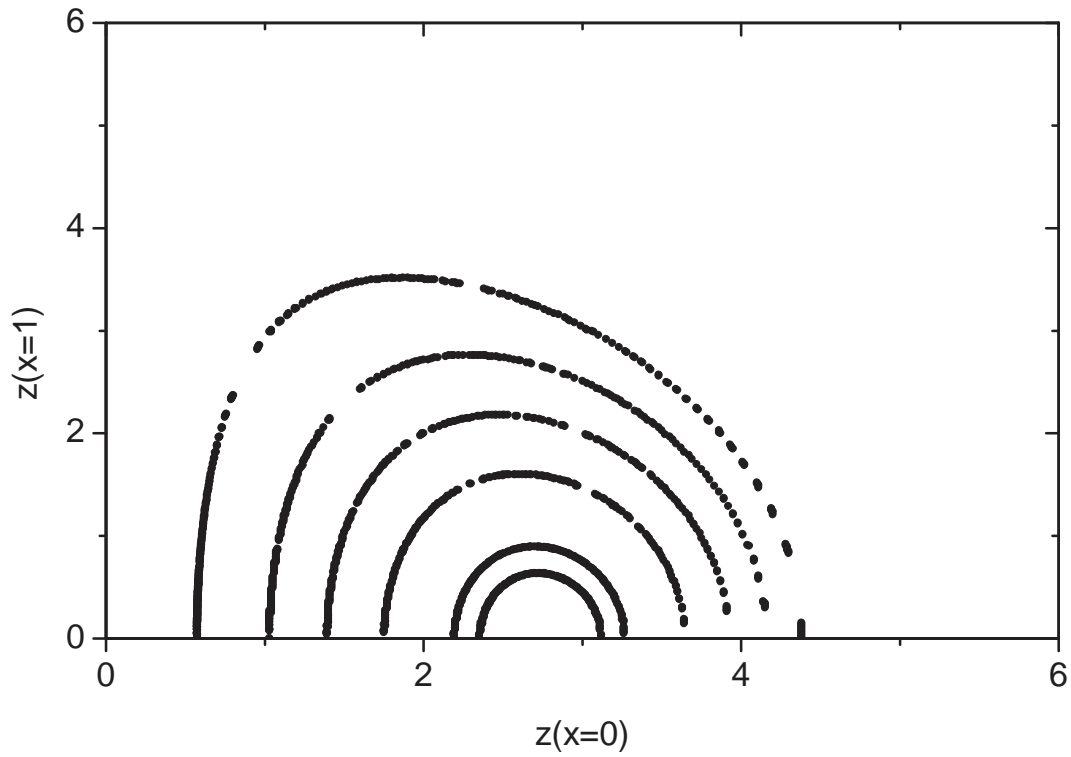


Fig. 2.— The poloidal magnetic field lines of  $R_0(z) = zj_1(z)$  L mode are shown in polar plots with increasing contour labels from outer to inner contours. These contours are shared by the poloidal rotation. The axes are labelled in  $z$  together with  $x = \cos \theta$ .

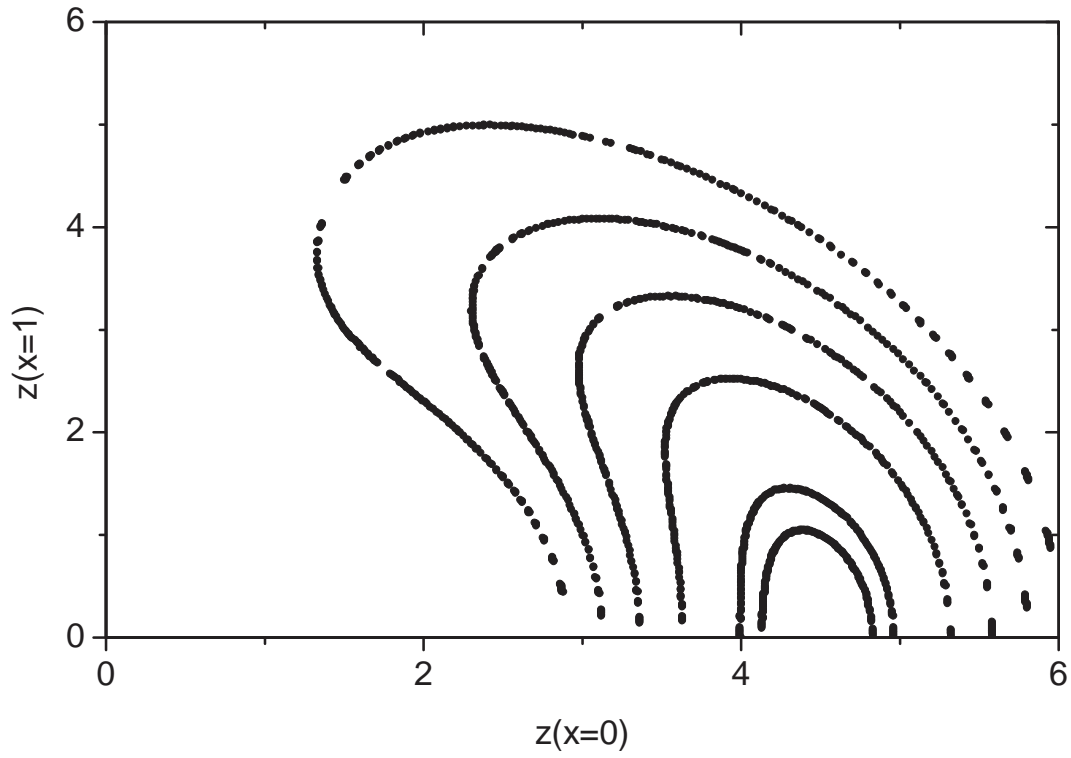


Fig. 3.— The poloidal magnetic field lines of  $R_0(z) = zy_1(z)$  H mode are shown in polar plots with increasing contour labels from outer to inner contours.

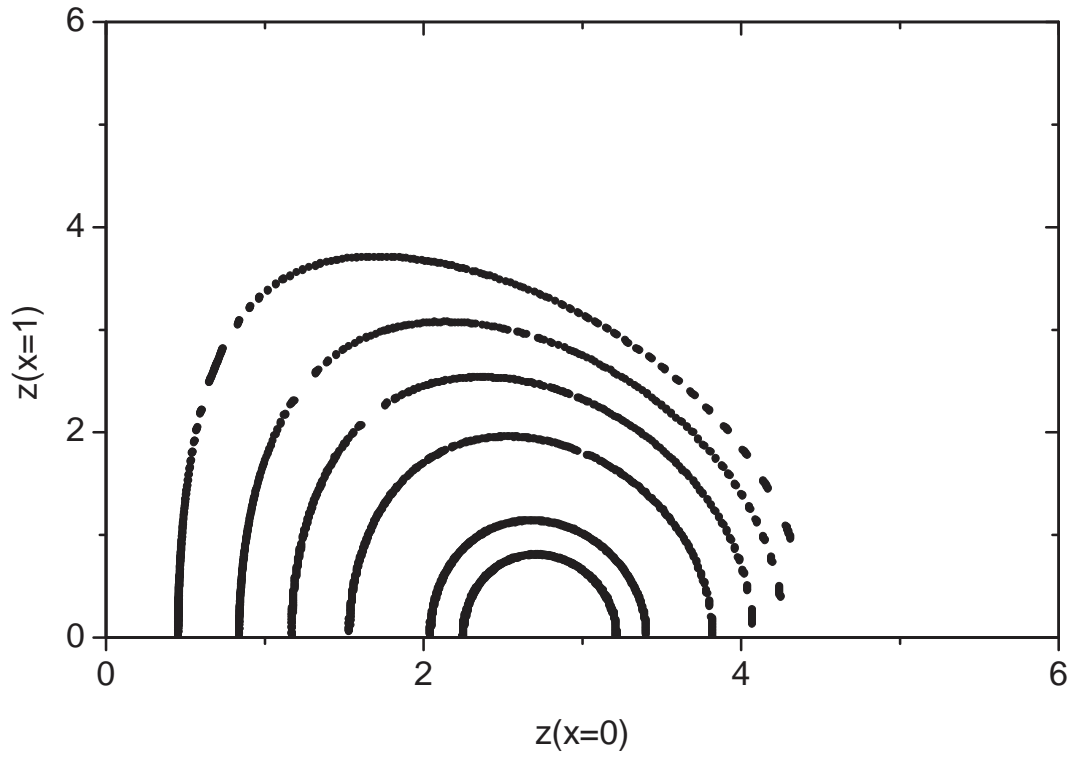


Fig. 4.— The mass density contours of  $R_0(z) = z j_1(z)$  L mode are shown in polar plots with increasing contour labels from outer to inner contours.

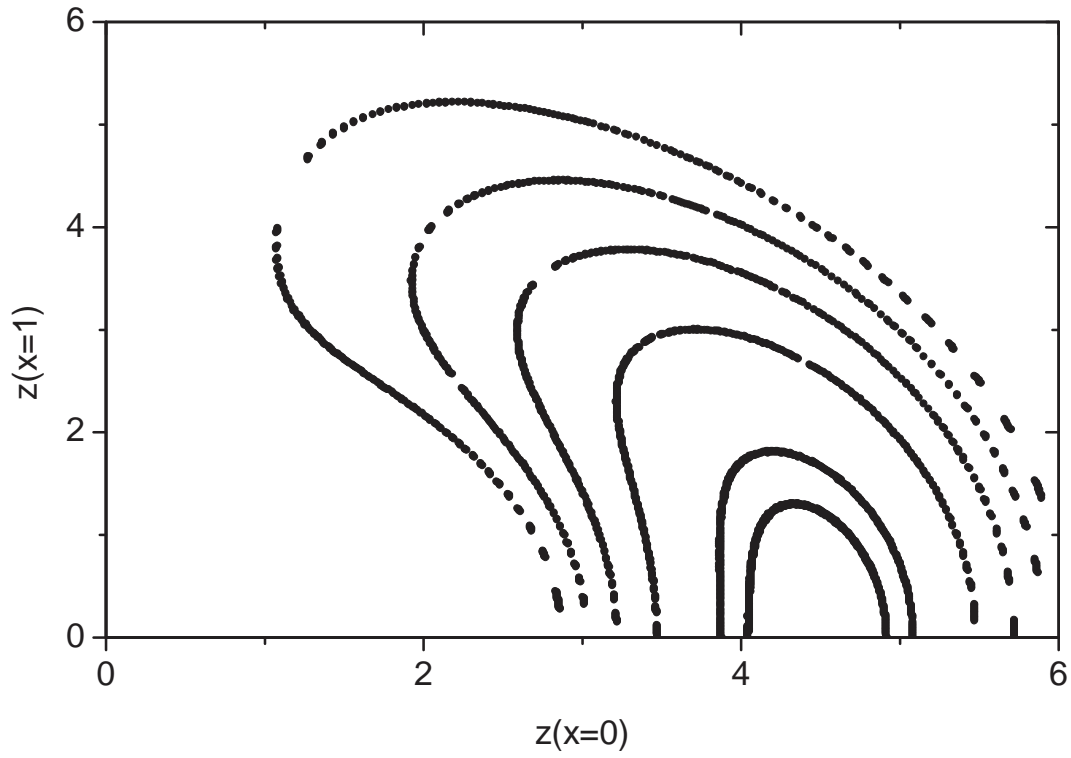


Fig. 5.— The mass density contours of  $R_0(z) = zy_1(z)$  R mode are shown in polar plots with increasing contour labels from outer to inner contours.

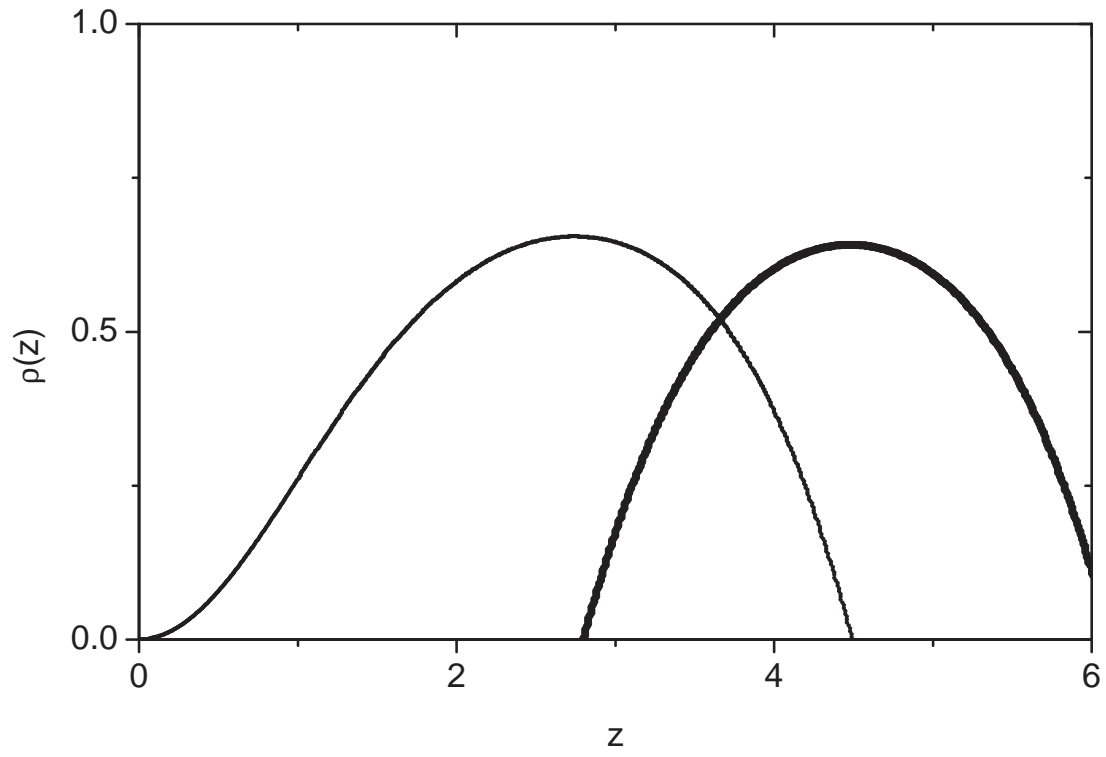


Fig. 6.— The mass densities along  $x = 0$  for  $zj_1(z)$  mode, in thin line, and  $zy_1(z)$  mode, in thick line, are plotted as a function of  $z$ .

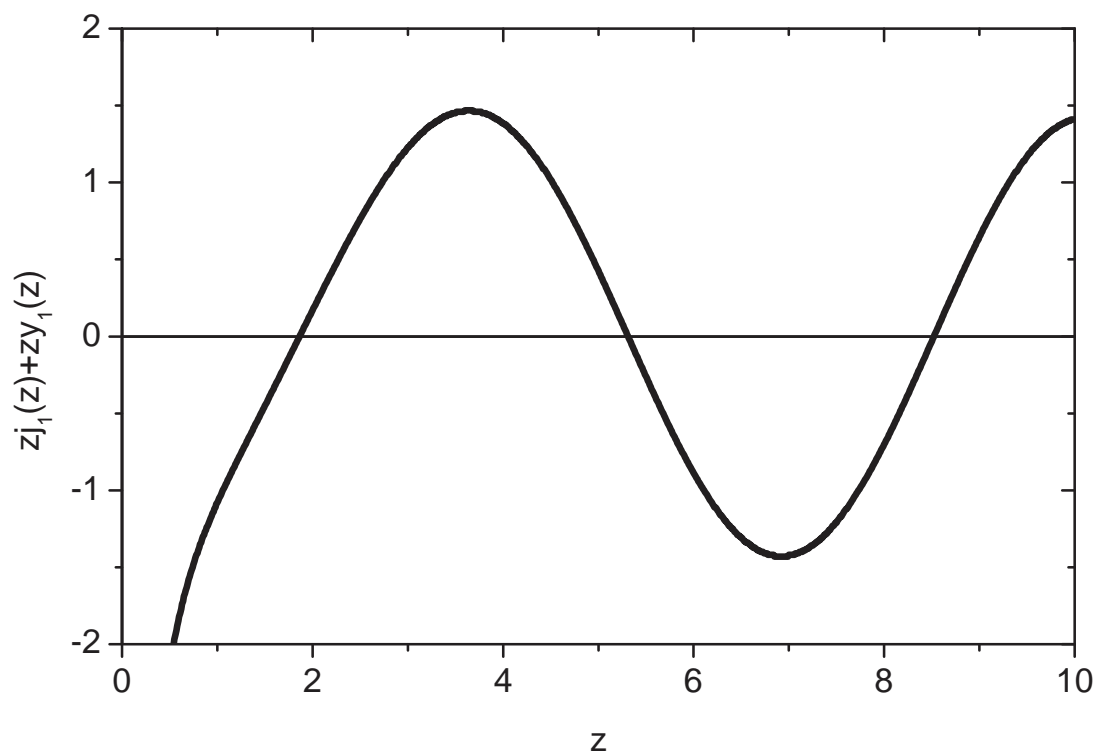


Fig. 7.— The function  $zj_1(z) + zy_1(z)$  is plotted as a function of  $z$  indicating  $z_1 = 1.9$  and  $z_2 = 5.3$ .